ACS APPLIED MATERIALS & INTERFACES

RESEARCH ARTICLE

www.acsami.org

Formation of Three-Dimensional Urchin-like α-Fe_2O_3 Structure and Its Field-Emission Application

Li-Chieh Hsu, Hsin-Chih Yu, Tai-Hsun Chang, and Yuan-Yao Li*

Department of Chemical Engineering, National Chung Cheng University, 168 University Road, Min-Hsiung, Chia-Yi 621, Taiwan

ABSTRACT: A three-dimensional urchin-like α-Fe_2O_3 microstructure is formed via a simple, template-free, and one-step thermal oxidation of Fe spheres in an air atmosphere at temperatures in the range of 300−450 °C. The urchin-like α-Fe_2O_3 microstructure consists of crystalline α-Fe_2O_3 nanoflakes grown perpendicularly on the surface of the sphere, a shell layer of α-Fe_2O_3/Fe_3O_4, and an Fe core. During the oxidation process, the nanoflakes germinate and grow from cracks in the oxidation layer on the surface. The length of the nanoflakes increases with oxidation time. The tip diameters of the nanoflakes are in ranges of 10−20 nm at 300 °C, 20−30 nm at 350 °C, and 40−60 nm at 400 °C; the length can reach up to a few micrometers. The field-emission characteristics of the samples are experimentally studied and simulated. The results show that the urchin-like emitter has a low turn-on field of 2.8 V/μm, high field-enhancement factor of 4313, excellent emission uniformity of over 4 cm^2, and good emission stability during a 24 h test.

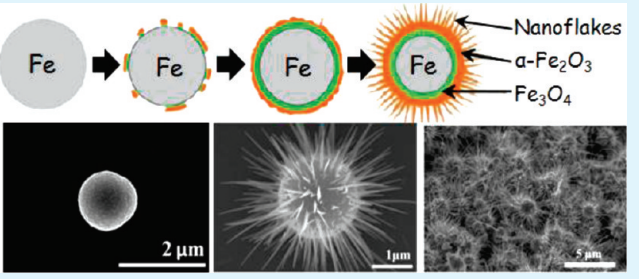

KEYWORDS: urchin-like α-Fe_2O_3, thermal oxidation, growth mechanism, field emission, Fe_2O_3 nanoflakes

INTRODUCTION

Hematite (α-Fe_2O_3) is a direct narrow band gap (2.1 eV) n-type semiconductor with a stable chemical state, unique magnetic properties,[1] and good thermal stability. α-Fe_2O_3 nanomaterials have been studied extensively in terms of their synthesis and applications in gas sensors,[2] water splitting,[3] photodetectors,[4] solar cells,[5] field-emission (FE) devices,[6,7] and field-effect transistors.[8] Many α-Fe_2O_3 nanostructures have been fabricated, such as nanowires (NWs),[1,6] nanobelts,[9] nanobridge,[4,8] hollow spheres,[10] shuttlelike nanostructures,[11] and fiber-in-tube and tube-in-tube nanostructures.[12] Recently, a three-dimensional (3D) urchin-like α-Fe_2O_3 structure has been fabricated via hydrothermal routes[13−20] using templates.

One-dimensional (1D) nanostructures have been extensively studied in FE applications due to their high aspect ratio and sharp tips. In addition to 1D nanostructures, the FE properties of 3D nanostructures such as ZnO nanotetrapods,[21] Eiffel-tower-shape AlN nanotips,[22] 6-fold-symmetrical AlN hierarchical nanostructures,[23] and urchin-like ZnO nanostructures[24] have also been investigated. These materials are composed of 1D sharp-tip nanostructures that point in various directions, which is beneficial for FE applications.[24]

In the present study, we report a simple one-step thermal oxidation process for synthesizing 3D urchin-like α-Fe_2O_3 structures. The morphology of the urchin-like α-Fe_2O_3 obtained here is different than those of urchin-like α-Fe_2O_3 materials reported in the literature.[18−20] The FE performance of the proposed urchin-like α-Fe_2O_3 structure was studied. A low turn-on field of 2.8 V/μm, high emission spot density (ESD) over a large area (2 × 2 cm^2), and good stability during a 24 h test were obtained.

EXPERIMENTAL SECTION

3D urchin-like α-Fe_2O_3 structures were grown via the oxidation of Fe spheres at various temperatures (250−400 °C). Fe powders (1−4.5 μm) with a purity of 97% (Sigma-Aldrich) were heated at a desired temperature in air from 0 to 12 h. The morphology and crystalline structure of the as-grown samples were examined by field-emission scanning electron microscopy (FE−SEM, HITACHI S−4800), high-resolution transmission electron microscopy (HR−TEM, Philips Tecnai F20), X-ray photoelectron spectroscopy (XPS, Kratos Axis Ultra DLD), micro-Raman spectroscopy (Jobin Yvon, Labram HR), and X-ray diffraction (XRD, RIGAKU Miniflex using Cu Kα radiation). The FE properties of the samples were investigated in a vacuum chamber at 1 × 10^{-6} Torr. The voltage was swept from 0 to 950 V and the emission current was monitored using a sourcemeter (Keithley 2410). Well-dispersed urchin-like α-Fe_2O_3 on Ag paste (2 × 2 cm^2) was used as the cathode. A phosphor screen was used as the anode to measure the emission current and to obtain fluorescence images. The cathode and anode were separated by a 150-μm-thick spacer.

RESULTS AND DISCUSSION

Figures 1(a) and 1(b) show an example of iron particles before and after thermal oxidation, respectively. The iron particle is spherical with a diameter of about 1 μm. After thermal treatment at 300 °C in air for 10 h (Figure 1b), high-density nanoflakes grew radially on the surface of the particle. The surface coverage density is about 2.5 × 10^{12} nanoflakes per square meter. For all

Received: May 15, 2011
Accepted: July 20, 2011
Published: July 20, 2011

the experimental conditions investigated, the nanoflakes were aligned perpendicularly to the surface of the sphere. The diameter and length of the nanoflakes were 10−20 nm and several micrometers, respectively. According to the SEM observation, the material can be considered as a 3D urchin-like structure. Figure 1c)demonstrates that a large number of urchin-like structures can be produced using iron spheres via a simple one-step air oxidation process. Figure 1d shows a nanoflake removed from the urchin-like material. The nanoflake has a high aspect ratio with a wide root tapering to a sharp tip. An HR−TEM image and the corresponding selected-area electron diffraction (SAED) pattern of the nanoflake are shown in Figure 1e and its inset, respectively. The analysis reveals that the nanoflake is a single rhombohedral structure of α-Fe_2O_3 with its growth direction along [110], which is parallel to the long axis of the nanoflakes. The fringe spacing of 0.251 nm agrees well with the interplanar spacing of the (110) plane of α-Fe_2O_3.

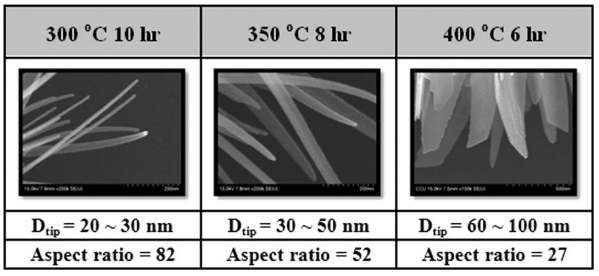

Figure 1. FE-SEM images of (a) Fe powder, (b) as-grown product, and (c) a large number of urchin-like structures. TEM image of (d) an α-Fe_2O_3 nanoflake, (e) HR-TEM image of an α-Fe_2O_3 nanoflake, and SAED pattern of α-Fe_2O_3 nanowire (inset).

Figure 2a shows the XRD patterns of Fe powder and the urchin-like α-Fe_2O_3 structure. The spectrum of the Fe powder is identified as that of α-Fe and the spectrum of the urchin-like structure indicates that the material is composed of Fe_3O_4, α-Fe_2O_3, and α-Fe. The presence of Fe_3O_4 was probably due to the incomplete oxidation of Fe powder. Fe is the core of the sphere. In addition, the high-intensity (110) peak can be regarded as the contribution from α-Fe_2O_3 nanoflakes, which was confirmed by HR−TEM analysis. For the surface analysis of the samples, Raman spectroscopy and XPS were conducted; the results are shown in Figure 2b (for Raman), 2(c), and 2(d) (for XPS). As expected, both spectra reveal that the surface composition of the material is mainly α-Fe_2O_3, which is chemically stable as it is the final oxidation state of Fe.

To understand the compositions of the surface and inner layers of the urchin-like structure, the samples were ultrasonically broken up. As shown in Figure 3a, the shell was removed from the main body of the material. The thickness of the shell is about 150 nm. The removed shell was collected and studied by TEM. Figure 3b shows a low-magnification TEM image of the shell of the urchin-like α-Fe_2O_3. The area marked with a dot-circle was further investigated by HR-TEM; the result is shown in Figure 3c. The shell is a single-crystal structure with a lattice spacing of 0.251 nm. The SAED pattern shown in the inset of Figure 3c indicates that the shell is a rhombohedral structure of α-Fe_2O_3. The nanoflakes and removed shell are thus confirmed to be single-crystal α-Fe_2O_3 structures. Figure 3d shows a SEM image of the core−shell interface enlarged from Figure 3a. As can

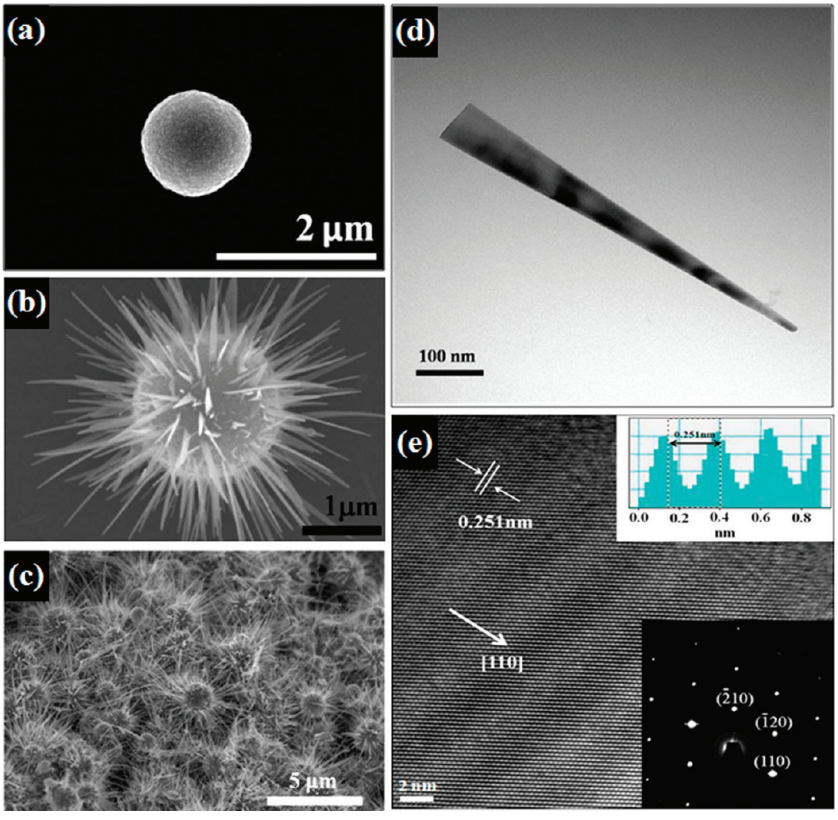

Figure 2. (a) XRD patterns of the urchin-like α-Fe_2O_3 structure and Fe powder, (b) Raman spectrum, and XPS profiles of the (c) O 1s region and (d) Fe 2p region for the urchin-like α-Fe_2O_3 structure.

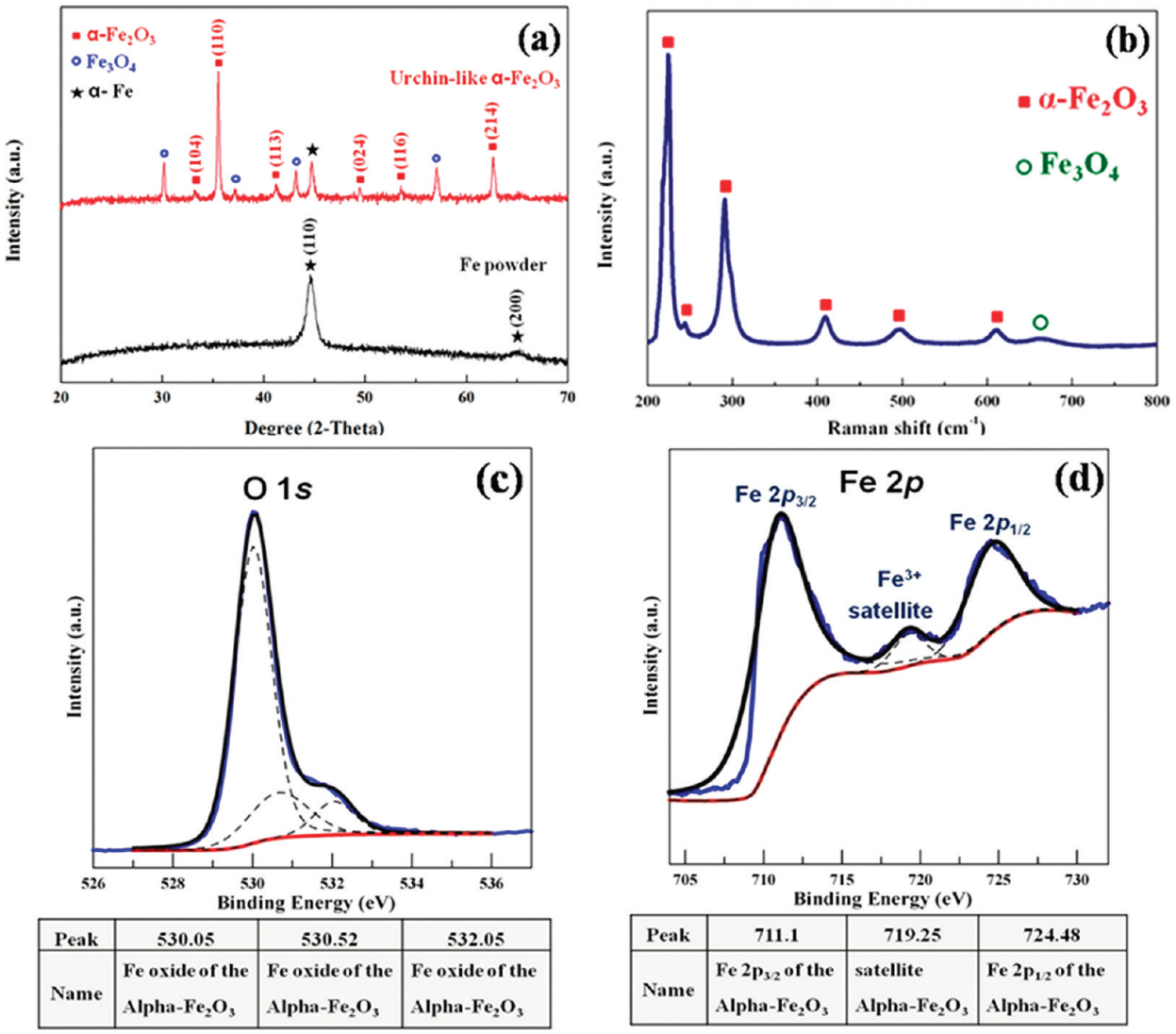

Peak	530.05	530.52	532.05
Name	Fe oxide of the Alpha-Fe_2O_3	Fe oxide of the Alpha-Fe_2O_3	Fe oxide of the Alpha-Fe_2O_3

Peak	711.1	719.25	724.48
Name	Fe $2p_{3/2}$ of the Alpha-Fe_2O_3	satellite Alpha-Fe_2O_3	Fe $2p_{1/2}$ of the Alpha-Fe_2O_3

Figure 3. (a) FE-SEM image of the core/shell/nanoflake structure of the urchin-like α-Fe_2O_3, (b) TEM image of the removed shell, (c) HR-TEM image and SAED pattern (inset) of the shell of the urchin-like α-Fe_2O_3, (d) high-magnification FE-SEM image of the core/shell structure, and (e) EDS mapping of Fe and O elements at the interface of the core/shell structure.

be seen, there are many small protrusions on the surface of the core. Figure 3e shows the fixed X-ray energy of Fe Kα and O Kα obtained by EDS mapping the area shown in Figure 3d. Green dots indicate the existence of the elements.[25] The densities of Fe in the shell and the core are almost the same. In contrast, the distribution of the O element can be divided into the oxygen-rich region (shell) and the oxygen-depleted region (surface of the core). The data implies that the shell (α-Fe_2O_3) has a higher oxygen concentration than that of the surface of the core. As a result, the composition of the surface of the core might not be Fe_2O_3 (O/Fe=1.5) but another form of iron oxide, which has a lower O/Fe ratio than that of Fe_2O_3. As the XRD results show that the urchin-like nanoflake structure consists of Fe, Fe_3O_4, and α-Fe_2O_3, we believe that the surface of the core is dominated by Fe_3O_4 (O/Fe = 1.3). The urchin-like material might thus consist of (from inside to outside); Fe core (no oxidation), Fe_3O_4 surface of the core (partial oxidation), α-Fe_2O_3 shell (complete oxidation), and α-Fe_2O_3 nanoflakes (selective oxidation of α-Fe_2O_3 in the [110] direction).

The growth mechanism of the urchin-like α-Fe_2O_3 structure by thermal oxidation has not been previously investigated. However, the synthesis of α-Fe_2O_3 NWs/flakes was discussed by Takagi[26] and in our previously study.[6,8] Since the growth temperature is much lower than the melting points of Fe (1538 °C), Fe_3O_4 (1538 °C), and α-Fe_2O_3 (1566 °C),[27] the vapor−liquid−solid (VLS) and vapor-solid (VS) mechanisms are not responsible for the nanoflake growth. The growth mechanism of nanoflakes is suggested to be selective directional growth via the interdiffusion of oxygen and iron atoms. Thus, the growth mechanism of the urchin-like α-Fe_2O_3 may be similar to the growth of α-Fe_2O_3 NWs. The growth mechanism of nanoflakes on a sphere was observed with the increase of the oxidation time. Figure 4 shows an example of the morphological change of an Fe sphere during thermal oxidation in air and the possible growth mechanism. Figure 4a shows the original iron sphere and Figure 4b shows the sphere after oxidation in air at 300 °C for 30 min. Worm-like protrusions can be seen on the surface. It is believed that these protrusions were iron oxides partially covering

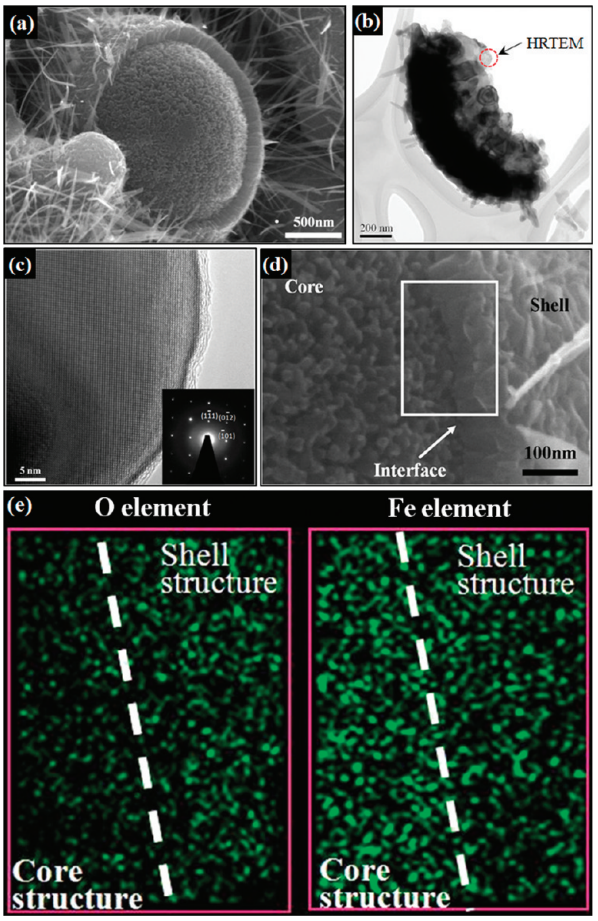

Figure 4. Schematic diagram and FE-SEM images of the formation of the urchin-like α-Fe_2O_3 nanostructure.

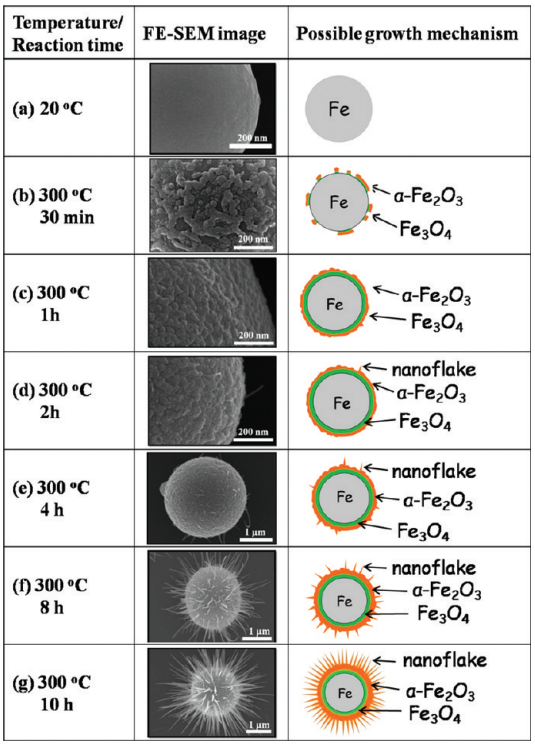

Figure 5. FE-SEM images of urchin-like α-Fe_2O_3 grown at 250, 300, 350, and 400 °C for 0, 2, 4, 6, 8, 10, and 12 h, respectively.

the surface of the sphere. After 1 h of the thermal process at 300 °C (Figure 4c), a rough oxide layer replaces the protrusions. The diffusion of oxygen atoms toward the core and the diffusion of inner iron atoms toward the surface increased the thickness of the oxide layer and decreased the core diameter of the iron sphere. The layer is believed to be a mixture of Fe_2O_3 and Fe_3O_4.[28] When the oxidation time reached 2 h, nanoflakes appeared in the cracks of the oxide layer, as shown in Figure 4d. We believe that the nanoflakes formed via selective directional oxidation (growth) because of the rapid oxidation rate of the [110] direction of iron oxide. Figures 4e−g show results for oxidation times of 4, 8, and 10 h, respectively; the length and the number of nanoflakes increased with oxidation time. The diameter of the urchin-like sphere increased due to an increase of the oxide shell thickness. In addition, the roots of the nanoflakes became wider with increasing oxidation time. For the thermal process at 300 °C, the length and the number of nanoflakes reached their maximum values after 10 h. As the thickness of the layer increased to a critical point, the interdiffusion of oxygen atoms and iron atoms was slowed down and eventually stopped. The tip diameters and lengths of nanoflakes were 30−50 nm and 1−2 μm, respectively.

The effects of oxidation temperature on the growth of the urchin-like α-Fe_2O_3 structure were investigated at oxidation temperatures of 250, 300, 350, and 400 °C for dwell times of 0−12 h, respectively. Figure 5 shows SEM images of the samples for various temperatures and times. The results show that the urchin-like nanoflake α-Fe_2O_3 structure forms at temperatures of 300 - 400 °C. The oxidation time required for the nanoflakes to form decreased with increasing temperature. The morphologies of the nanoflakes obtained at temperatures of 300, 350, and 400 °C were slightly different in terms of the diameter and length. According to our observations, the morphological differences are due to differences in the oxidation temperature (or oxidation rate), which led to different degrees of roughness of the sphere in the early stage of the oxidation process and affected the growth behavior of the nanoflakes. As shown in the four SEM images in the first column (Figure 5), which correspond to samples processed at 250, 300, 350, and 400 °C, respectively, without a dwell time, the surface roughness increased with increasing oxidation temperature. The surface roughness affected the diameters of the nanoflakes; a rougher surface resulted in a larger diameter of the nanoflakes. For example, the tip diameters of the nanoflakes on the spheres are in ranges of 10−20, 20−30, and 40−60 nm for oxidation temperatures of 300, 350, and 400 °C, respectively. As previously mentioned, the nanoflakes grew from the surface cracks. A rougher surface created larger cracks, which led to the formation of nanoflakes with wider diameters. Figure 5 also shows that the length and the number of nanoflakes increased with increasing oxidation time. No significant changes were found in terms of the diameter, length, and density of the nanoflakes after 10 h at 300 °C, 8 h at 350 °C, and 6 h at 300 °C. The diameter, length and density of the α-Fe_2O_3 nanoflakes increase with oxidation time for a given oxidation temperature. For example, the tip diameter of the α-Fe_2O_3 nanoflakes increased to 20−30 nm (10 h of oxidation) from 10−20 nm (6 h of oxidation) at a synthesis temperature of 300 °C. The diameter and the density of the α-Fe_2O_3 nanoflakes increase with oxidation temperature for a given oxidation time. For example,

for an oxidation time of 6 h, the tip diameter of the α-Fe_2O_3 nanoflakes increased to 60−100 nm (synthesis temperature of 400 °C) from 10−20 nm (synthesis temperature of 300 °C). The morphology of the α-Fe_2O_3 nanostructure changed from nanowires to nanoflakes with increasing oxidation temperature. Table 1 summarized the relationship of the length, diameter, and aspect ratio of the NWs or nanoflakes for various oxidation temperatures.

The field-emission properties of the urchin-like α-Fe_2O_3 structure were investigated. Figure 6(a) shows the dispersion of the urchin-like α-Fe_2O_3 on Ag film. The Fe powder was dispersed on precoated Ag paste by an air spray gun at first. After the thermal process (300 °C, 10 h), urchin-like α-Fe_2O_3 structures formed on the Ag film (Figure 6a). The distance between each urchin-like α-Fe_2O_3 particle was 20−40 μm. Figure 6b shows a cross-section image of the urchin-like emitter on the substrate. As can be seen, the urchin-like α-Fe_2O_3 structure was embedded in the Ag film, which indicates good contact with the conductive Ag layer; good field-emission performance is thus expected. In addition, the radial feature of the nanoflake structure ensures that some of the emitters face the anode, so that the cathode does not require a tapping process,[29] which is used to lift up the tips of the emitters embedded in the conductive layer after the screen printing of the emitters. The field-emission current density (J) versus electrical field (E) curve is shown in Figure 6c. The turn-on field (defined as the applied field attained to an emission current density of 10 μA/cm^2) is about 2.8 μm/V, which is better than that of α-Fe_2O_3 nanoflakes/NWs reported in the literature.[6] The Fowler−Nordheim (F−N) equation[21] was employed to analyze the field-emission properties of the urchin-like α-Fe_2O_3:

$$J = A\frac{(\beta E)^2}{\varphi} e^{(-B\varphi^{3/2}/\beta E)} \quad (1)$$

where J is the emission current density; E is the electrical field; φ is the work function of α-Fe_2O_3 (5.6 eV [6]); $A = 1.54 \times 10^{-6}$ AeVV^{-2}; and $B = 6.83 \times 10^3$ eV$^{-3/2}$ V μm^{-1}. β is the field-enhancement factor, which depends on the morphology and the crystal structure of the emitters. The inset of Figure 6c shows the F−N plot of $1/E$ versus $\ln(J/E^2)$ of the urchin-like α-Fe_2O_3 emitters. The linear relationship of $1/E$ versus $\ln(J/E^2)$ indicates that the field-emission behavior fits the F−N mechanism. β was obtained as 4313. In our previously study,[6] which used Fe film for the growth of Fe_2O_3 nanoflakes/NWs, the β of α-Fe_2O_3 NWs was 1754, which is much lower than that obtained in the present study. We believe that α-Fe_2O_3 nanoflakes grown on the spherical support have a higher field-enhancement factor (β) than that of α-Fe_2O_3 NWs on the planar support. This implies that field-emission performance strongly depends on the structure of the support (sphere or film).

To verify the effect of the support structure, the electric field of the emitter was analyzed using a SIMION software simulation. Electron tunneling is affected by the local electric field, which depends on the morphology (such as the diameter and the aspect ratio) of the emitters and the spacing between the emitters.[30] Figure 7 shows the electric-field contours around the emitters. The field distributions around nanoflakes (diameter = 15 nm, length = 2.5 μm, spacing between nanoflakes = 350 nm) on a spherical support (diameter = 4.5 μm) and on a planar support are shown in panels a and b in Figures 7, respectively. The results show that the local electric field of the tip was 45.77 V/μm at point 1 for the urchin-like structure, and 29.73 V/μm at point 2 for the nanoflake on the planar support. According to the electric field analysis, the local electric field of the nanoflakes on the spherical support was much higher than that of the nanoflakes on the planar support. The higher local electric field enhanced the rate of electron tunneling,[30] which led to a lower turn-on voltage and higher β. The local electric field can thus be amplified by changing the structure of the support.

Figure 8 shows fluorescence images of field emission (4 cm^2) for the urchin-like α-Fe_2O_3 emitters with various applied electric

Table 1. Relationship of the Diameter and Aspect Ratio of Nanoflakes for Various Oxidation Temperatures

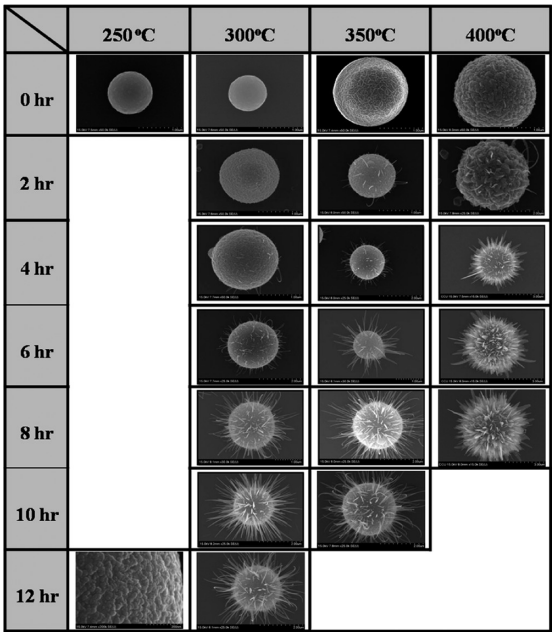

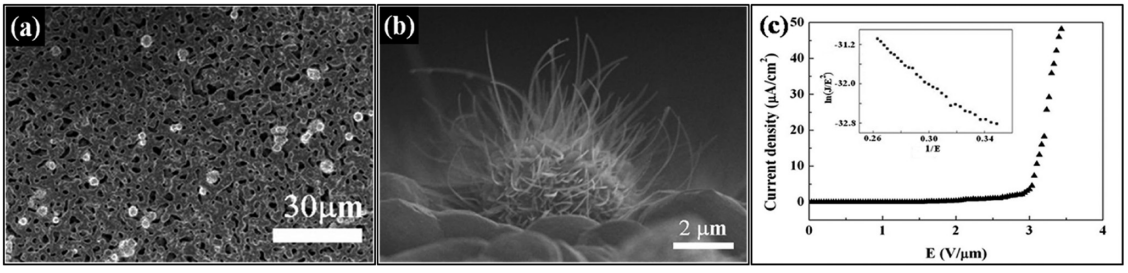

Figure 6. FE-SEM images of urchin-like α-Fe_2O_3 grown at 300 °C for 10 h. (a) Top-view and (b) cross-section of the urchin-like α-Fe_2O_3 on Ag paste. (c) Current density as a function of the electrical field for the urchin-like α-Fe_2O_3; the inset corresponds to the Fowler−Nordheim (F−N) plot.

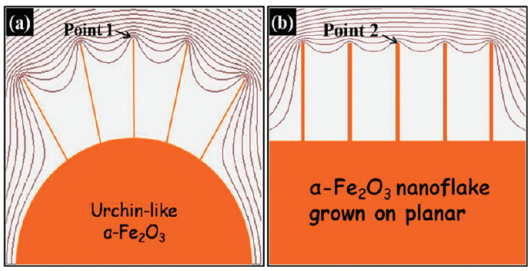

Figure 7. Schematic of the simulated field distribution around the α-Fe_2O_3 nanowires on a (a) spherical support and (b) planar support.

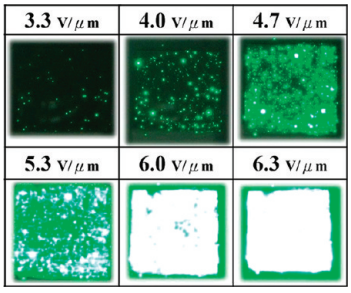

Figure 8. Fluorescence images (2×2 cm^2) of the urchin-like α-Fe_2O_3 with applied fields of 3.3, 4.0, 4.7, 5.3, 6.0, and 6.3 V/μm, respectively.

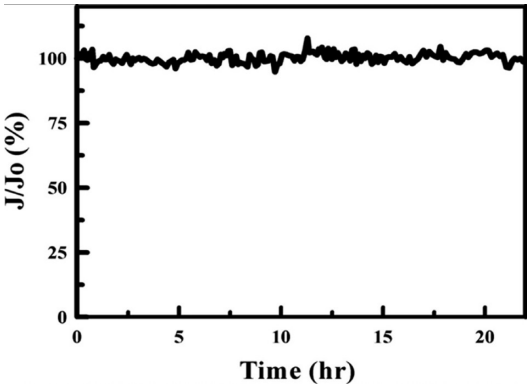

Figure 9. Representative emission stability curve of the urchin-like α-Fe_2O_3 nanostructure at an applied electric field of 6.0 V/μm.

fields. It can be seen that the emission spot density (ESD) is directly proportional to the current density. EDS increased with increasing applied electric field. Due to the good dispersion and high efficiency of the urchin-like α-Fe_2O_3 emitters, the ESD increased in a narrow range of the applied field (5.3−6.0 V/μm). Almost all the phosphors were excited under an applied field of 6.3 V/μm, with bright spots uniformly distributed on the screen. This excellent emission homogeneity is important for display and lighting applications.

The emission stability of urchin-like α-Fe_2O_3 was also investigated. Figure 9 shows the current density over a long period of time. The applied field was fixed at 6.0 μm/V for 24 h. No obvious degradation of the emission performance was observed, and the fluctuation of the emission current was less than 4% throughout the continuous high-current operation. The good field-emission stability of the urchin-like α-Fe_2O_3 can be attributed to (1) the chemical stability of the α-Fe_2O_3 (α-Fe_2O_3 is the most stable iron oxide in an ambient environment) and (2) its unique structure (urchin-like α-Fe_2O_3 nanoflakes structures). The low turn-on field, high β, high ESD, and good emission stability of the urchin-like α-Fe_2O_3 make it a promising candidate for field-emission devices.

CONCLUSION

A simple, template-free, and one-step thermal oxidation of Fe spheres for the synthesis of a 3D urchin-like α-Fe_2O_3 microstructure was reported. The material was constructed of α-Fe_2O_3 single-crystalline nanoflakes perpendicular to the surface, a shell layer of α-Fe_2O_3 and Fe_3O_4, and an Fe core. The oxidation temperature played an important role in the formation of a rough surface layer, which affected the diameter of the nanoflakes. A field-emission study using the urchin-like α-Fe_2O_3 as emitters shows that the emitters have a low turn-on field of 2.8 V/μm, a high β of 4313, a high ESD over a large area (2×2 cm^2), and good emission stability during a 24-h test. These experimental results indicate that the urchin-like α-Fe_2O_3 is a candidate for field-emission devices.

AUTHOR INFORMATION

Corresponding Author

*Phone: +886-5-2720411, ext. 33403. Fax: +886-5-2721206. E-mail: chmyyl@ccu.edu.tw.

REFERENCES

(1) Hsu, L. C.; Li, Y. Y.; Lo, C. G.; Huang, C. W.; Chern, G. *J. Phys. D: Appl. Phys.* **2008**, *41*, 185003.
(2) Chauhan, P.; Annapoorni, S.; Trikha, S. K. *Thin Solid Films* **1999**, *346*, 266.
(3) Cesar, I.; Kay, A.; Gonzalez Martinez, J. A.; Grätzel, M. *J. Am. Chem. Soc.* **2006**, *128*, 4582.
(4) Hsu, L. C.; Kuo, Y. P.; Li, Y. Y. *Appl. Phys. Lett.* **2009**, *94*, 133108.
(5) Beermann, N.; Vayssieres, L.; Lindquist, S.-E.; Hagfeldt, A. *J. Electrochem. Soc.* **2000**, *147*, 2456.
(6) Hsu, L.-C.; Li, Y.-Y.; Hsiao, C.-Y. *Nanoscale Res. Lett.* **2008**, *3*, 330.
(7) Yu, T.; Zhu, Y.; Xu, X.; Yeong, K.-S.; Shen, Z.; Chen, P.; Lim, C.-T.; Thong; John, T.-L.; Sow, C.-H. *Small* **2006**, *2*, 80.
(8) Hsu, L. C.; Li, Y. Y. *Appl. Phys. Lett.* **2008**, *93*, 083113.
(9) Wen, X. G.; Wang, S. H.; Ding, Y.; Wang, Z. L.; Yang, S. H. *J. Phys. Chem. B* **2005**, *109*, 215.
(10) Guan, J.; Mou, F.; Sun, Z.; Shi, W. *Chem. Commun* **2010**, *46*, 6605.
(11) Ngo, A. T.; Pileni, M. P. *J. Appl. Phys.* **2002**, *92*, 4649.
(12) Mou, F.; Guan, J.-g.; Shi, W.; Sun, Z.; Wang, S. *Langmuir* **2010**, *26*, 15580.
(13) Tong, G.; Guan, J.; Zhang, Q. *Mater. Chem. Phys.* **2011**, *127*, 371.
(14) Tong, G.; Guan, J.; Xiao, Z.; Huang, X.; Guan, Y. *J. Nanopart. Res.* **2010**, *12*, 3025.
(15) Tong, G.; Wu, W.; Guan, J.; Qian, H.; Yuan, J.; Li, W. *J. Alloy. Compd.* **2011**, *509*, 4320.
(16) Huang, X.; Guan, J.; Xiao, Z.; Tong, G.; Mou, F.; Fan, X. a. *J. Colloid Interface Sci.I* **2011**, *357*, 36.
(17) Mou, F.; Guan, J.; Xiao, Z.; Sun, Z.; Shi, W.; Fan, X.-a. *J. Mater. Chem.* **2011**, *21*, 5414.
(18) Zhu, L. P.; Xiao, H. M.; Liu, X. M.; Fu, S. Y. *J. Mater. Chem.* **2006**, *16*, 1794.
(19) Zhang, Y. P.; Chu, Y.; Dong, L. H. *Nanotechnology* **2007**, *18*, 435608.
(20) Du, D.; Cao, M. *J. Phys. Chem. C* **2008**, *112*, 10754.

(21) Qu, K.; Li, C.; Hou, K.; Yang, X. X.; Zhang, J.; Lei, W.; Zhang, X. B.; Wang, B. P.; Sun, X. W. *Appl. Phys. Lett.* **2008**, *93*, 253501.
(22) Tang, Y. B.; Cong, H. T.; Chen, Z. G.; Cheng, H. M. *Appl. Phys. Lett.* **2005**, *86*, 233104.
(23) Zhang, F.; Wu, Q.; Wang, X. B.; Liu, N.; Yang, J.; Hu, Y. M.; Yu, L. S.; Wang, X. Z.; Hu, Z.; Zhu, J. M. *J. Phys. Chem. C* **2009**, *113*, 4053.
(24) Jiang, H.; Hu, J. Q.; Gu, F.; Li, C. Z. *Nanotechnology* **2009**, *20*, 055706.
(25) Cheng, C. L.; Ma, Y. R.; Chou, M. H.; Huang, C. Y.; Yeh, V.; Wu, S. Y. *Nanotechnology* **2007**, *18*, 245604.
(26) Tadagi, R. *J. Phys. Soc. Jpn.* **1957**, *12*, 1212.
(27) Rao, P. M.; Zheng, X. L. *Nano Lett.* **2009**, *9*, 3001.
(28) Zhao, Y.; Li, Y. H.; Ma, R.; Roe, M.; McCartney, D.; Zhu, Y. *Small* **2006**, *2*, 422.
(29) Jeong, H. J.; Choi, H. K.; Kim, G. Y.; Song, Y. I.; Tong, Y.; Lim, S. C.; Lee, Y. H. *Carbon* **2006**, *44*, 2689.
(30) Han, S. W.; Lee, M. H.; Ihm, J. *Phys. Rev. B* **2002**, *65*, 085405.